nature biotechnology

Multifunctional fibers for simultaneous optical, electrical and chemical interrogation of neural circuits *in vivo*

Andres Canales[1,4], Xiaoting Jia[2,4], Ulrich P Froriep[2–4], Ryan A Koppes[2,4], Christina M Tringides[1], Jennifer Selvidge[1], Chi Lu[1], Chong Hou[1], Lei Wei[2], Yoel Fink[1,2] & Polina Anikeeva[1,2]

Brain function depends on simultaneous electrical, chemical and mechanical signaling at the cellular level. This multiplicity has confounded efforts to simultaneously measure or modulate these diverse signals *in vivo*. Here we present fiber probes that allow for simultaneous optical stimulation, neural recording and drug delivery in behaving mice with high resolution. These fibers are fabricated from polymers by means of a thermal drawing process that allows for the integration of multiple materials and interrogation modalities into neural probes. Mechanical, electrical, optical and microfluidic measurements revealed high flexibility and functionality of the probes under bending deformation. Long-term *in vivo* recordings, optogenetic stimulation, drug perturbation and analysis of tissue response confirmed that our probes can form stable brain-machine interfaces for at least 2 months. We expect that our multifunctional fibers will permit more detailed manipulation and analysis of neural circuits deep in the brain of behaving animals than achievable before.

Simultaneous probing and manipulation of neurons during behavioral tasks is critical to the understanding of neural computation in the brain and pathologies of the nervous system[1,2]. Over the past two decades, advances in materials processing yielded numerous neural recording devices with ever increasing resolution. In addition to recording capabilities, the analysis of neural circuits requires the stimulation of specific cells with millisecond precision. The recent development of optogenetics[3] made studies of the neural basis of learning[4] and decision making[5] possible. *In vivo* identification of cell types could be further facilitated by the infusion of pharmacological compounds[6]. Thus, there is a drive to integrate optical and pharmacological interrogation capabilities with neural probes for recording[7–9]. However, as most multifunctional devices are based on the existing recording probe architectures, they tend to suffer from the same limitations.

Commonly used electrophysiological probes[10–14] are based on materials with elastic moduli significantly exceeding those of neural tissues ($E \approx 10$–100 GPa, versus E values in the range of kilopascals to megapascals[15,16]). Although these devices are useful in short-term experiments[17], their long-term applications are limited by a decrease in signal-to-noise ratio (SNR) and the number of cells monitored over time. It has been suggested that these limitations stem from the formation of glial scars and neuronal death surrounding the electrodes[17,18]. Several factors, including breach of the blood-brain barrier[19] (BBB), disruption of glial networks[20] and tissue damage due to micromotion[21] of the brain with respect to the implant, are thought to contribute to the failure of probes in long-term experiments.

Recently, microcontact printing and micromachining techniques were used to develop neural probes on flexible substrates[22–25]. The resolution of contact printing methods, however, does not allow for the integration of multiple electrodes or drug delivery systems without a significant increase in device dimensions. Hence, there remains a need for flexible, multifunctional neural probes.

Here we present a class of neural probes fabricated from polymer, metal and composite materials by means of a thermal drawing process (TDP) traditionally employed in optical fiber production[26–30]. We successfully used our fiber probes for simultaneous optogenetic stimulation, neural recording and drug delivery in freely moving mice. Moreover, histological assessment of the tissue response showed that our fiber probes yielded stable multifunctional interfaces with the brain. The TDP is a highly versatile fabrication method that may yield thousands of probes from a single inexpensive preform, thereby reducing the cost barrier associated with combining behavioral experiments with multimodal neural interrogation.

RESULTS

During the TDP, a macroscopic template of the fiber, termed the 'preform', fabricated by macroscale machining, is heated and stretched into a fiber, yielding a reduction of cross-sectional features by up to 200 times. Consecutive drawing steps can be applied to reduce the feature dimensions even further[27].

Although the TDP is commonly applied to glasses[26,28], we took advantage of recent developments in multimaterial fiber technology[29] to create polymer and polymer-metal structures. To produce devices with elastic properties comparable to those of neural tissue, we evaluated a materials toolbox (**Supplementary Table 1**) consisting of polymers commonly used in medical devices (poly(etherimide) (PEI), poly(phenylsulfone) (PPSU), polycarbonate (PC) and cyclic

[1]Department of Materials Science and Engineering, Massachusetts Institute of Technology, Cambridge, Massachusetts, USA. [2]Research Laboratory of Electronics, Massachusetts Institute of Technology, Cambridge, Massachusetts, USA. [3]Simons Center for the Social Brain, Massachusetts Institute of Technology, Cambridge, Massachusetts, USA. [4]These authors contributed equally to this work. Correspondence and requests for samples should be addressed to P.A. (anikeeva@mit.edu).

Received 4 August 2014; accepted 10 November 2014; published online 19 January 2015; doi:10.1038/nbt.3093

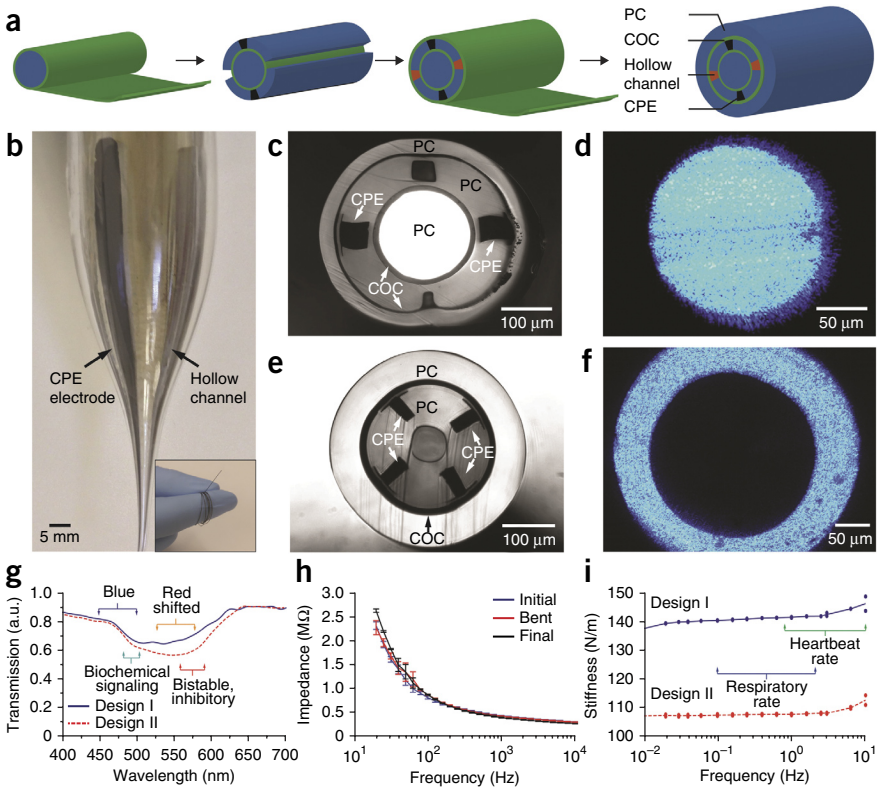

Figure 1 Multimodality fiber probe fabrication and characterization. (**a**) A schematic showing the fabrication steps of the preform for multimodality fiber probes (design I). (**b**) A photograph of the design I preform at the transition part where it was drawn into the fiber. Inset: a photograph showing a section of the drawn fiber wrapped around a finger. (**c**,**e**) Cross-sectional optical images of the design I (**c**) and design II (**e**) multimodality probe tips. (**d**,**f**) Cross-sectional optical images of the light (laser wavelength $\lambda = 473$ nm) profile coupled into the core of the design I (**d**) and the outer layer of the design II (**f**) probes. (**g**) Transmission spectra of multifunctional fiber designs I (blue solid line) and II (red dashed line) indicate their compatibility with activation wavelengths of the diverse palette of opsins[46]. (**h**) Impedance spectroscopy of a multimodality probe (design I) electrode. There are no obvious differences among the values measured before (blue), during (red) and after (black) 90° bending of the probe at a 4-mm radius of curvature (lines and bars indicate mean and s.d.; $n = 10$ measurements). (**i**) Graph showing the measured bending stiffness for designs I (blue solid line) and II (red dashed line) at different frequencies, including those of respiration and heartbeat across different mammals. The displacement amplitude was 50 µm.

olefin copolymer (COC))[30,31], a polymer composite (conductive polyethylene (CPE)), and a low-melting-temperature metal (tin (Sn)). Because materials constituting the preform are heated together, they must possess sufficiently low viscosities (<10^7 P) at the draw temperature, allowing for continuous, simultaneous flow. Thus, materials should possess similar glass transition (T_g, amorphous materials) and melting temperatures (T_m, crystalline materials)[29]. Taking this into account, we used the TDP to fabricate multifunctional neural probes with varied geometries based on PC-COC-CPE and PPSU-PEI-Sn material combinations.

Multimodality all-polymer fiber probes

We first used the TDP to combine optical stimulation, drug delivery and neural recording capabilities in multimodality probes. These probes consist exclusively of polymers and polymer composites with elastic moduli lower than those of traditionally used semiconductors, glasses and high-melting-temperature metals.

Because PC, COC and CPE possess similar T_g and T_m values, they can be processed simultaneously in the TDP (**Supplementary Table 1**). PC and COC exhibit low absorption in the visible spectrum[32,33], and the difference between their refractive indexes permits light confinement within PC, whereas CPE serves as a recording electrode.

Here we demonstrate two designs with optical and pharmacological delivery features: design I, which incorporates a cylindrical waveguide, two microfluidic channels and two electrodes; and the thinner, concentric design II, which integrates one microfluidic channel, four electrodes and a surrounding waveguide.

Following its fabrication, a preform with optical and pharmacological delivery features (design I) (**Fig. 1a**) was annealed and drawn (**Fig. 1b**) into a ~500-m-long, flexible fiber (**Fig. 1b**, inset) with the cross-sectional geometry of the preform, but with dimensions reduced by a factor of ~100 (**Fig. 1c**,**d**). The dimensions of the fiber can be reduced and the number of recording sites increased by using a concentric structure (design II) (**Fig. 1e**,**f**).

As predicted by the refractive index contrast (**Supplementary Table 1**), light transmission was confined primarily to the innermost PC core in design I (**Fig. 1d**) and to the outermost PC layer in design II (**Fig. 1f**). Transmission spectroscopy confirmed the utility of the probes for optical guidance in the visible range (400–700 nm) (**Fig. 1g**). Because optogenetic experiments often involve channelrhodopsin 2 (ChR2)[3], we further quantified optical transmission along the multimodality probes at the ChR2 peak activation wavelength $\lambda = 473$ nm (**Supplementary Fig. 1**). Optical losses were 2.7 dB/cm (design I) and 1.6 dB/cm (design II), 2.4 to 4 times lower than those of previously reported polymer-based probes[8]. With the transmission spectra in **Figure 1g**, optical losses can be extrapolated to the desired wavelength.

The impedance of the multimodality probe electrodes at 1 kHz varied between 0.5 and 2.5 MΩ (design I) and between 3 and 5 MΩ (design II), consistent with CPE resistivity (**Fig. 1h**). The observed variability in impedance could stem from geometric factors at the fiber tip.

We confirmed microfluidic channel utility at injection rates of 1–100 nl/s. The drug delivery modality was not affected by 90° bending deformation of the probes (**Supplementary Fig. 2**). We further confirmed the injection capability by infusing Evans Blue through design I multimodality probes into medial prefrontal cortices (mPFCs) of wild-type (WT) mice (**Supplementary Fig. 3**).

We hypothesized that, in the context of tissue micromotion[21], the bending stiffness is more relevant than the elastic modulus, since the probes are expected to be fixed to the skull and are not anticipated to experience compressive or tensile stress. Although our probes are flexible and maintain their functions under significant deformations (**Fig. 1h** and **Supplementary Figs. 2**, **4** and **5**), we used a dynamic mechanical analyzer in single-cantilever mode to quantify the bending stiffness

of 1.3-cm fibers in the frequency range of mammalian locomotion, respiration and heartbeat (0.01–10 Hz) (**Fig. 1i**). We found that multimodality probe designs I and II exhibited bending stiffness values of 136–149 N/m and 107–115 N/m, respectively, which are substantially lower than that of silica fibers of comparable dimensions.

In vivo electrophysiology with multimodality fiber probes

As ChR2 mediates optogenetic excitation and is widely used in behavioral and systems neuroscience[34], we investigated the performance of multimodality fiber probes in the mPFC of *Thy1-ChR2-YFP* mice expressing ChR2 across the nervous system[35].

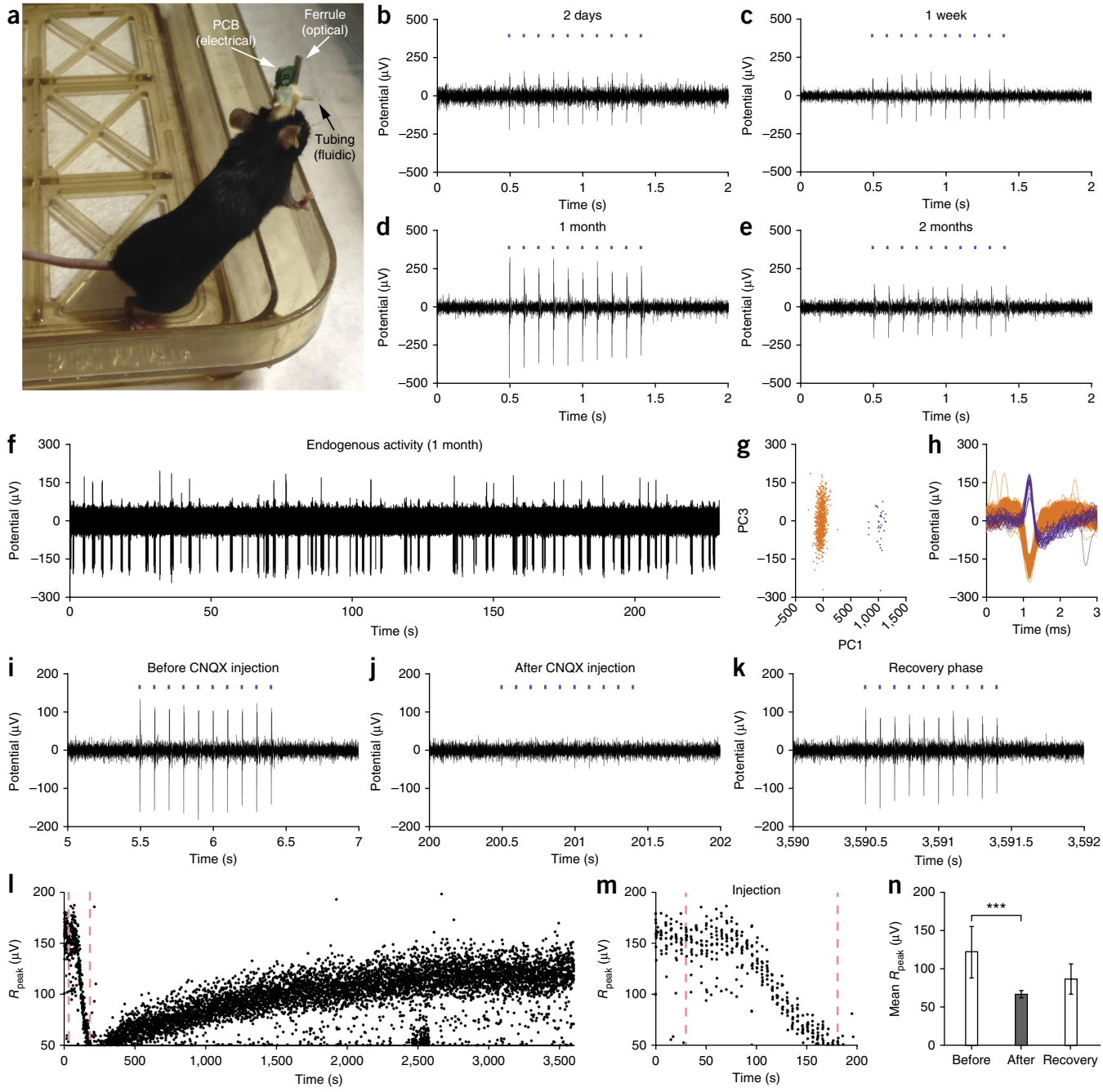

Figure 2 Multimodality probes allow for chronic implantation; single-unit resolution; and simultaneous electrophysiological recording, optogenetic stimulation and drug delivery. (**a**) Multimodality probes (design I) were implanted into the mPFC of transgenic *Thy1-ChR2-YFP* mice. (**b**–**e**) Simultaneous optogenetic stimulation (5-ms pulse width, 10 Hz, 1-s trial duration; blue marks indicate laser onsets) and electrophysiological recording was performed (**b**) 2 days, (**c**) 1 week, (**d**) 1 month and (**e**) 2 months after implantation. (**f**) Endogenous activity 1 month after implantation containing two separable neuronal units. (**g**) Principal-component analysis (PCA) of the two units in **f**. (**h**) Action-potential shapes of the two units in **f**. (**i**–**k**) Electrophysiological recording with design I multimodality probe (**i**) before, (**j**) 20 s after and (**k**) 3,410 s after injection of CNQX during optogenetic stimulation (10 Hz). (**l**,**m**) R_{peak} values of each detected spike reveal a decrease in spike amplitudes during CNQX injection (pink dashed vertical lines; zoomed-in view in **m**), followed by a recovery phase. (**n**) Comparison of the means of the R_{peak} values for the three different phases shows a significant difference between the before-injection and after-injection phases (***$P < 5 \times 10^{-12}$, $n = 3$, Student's *t*-test).

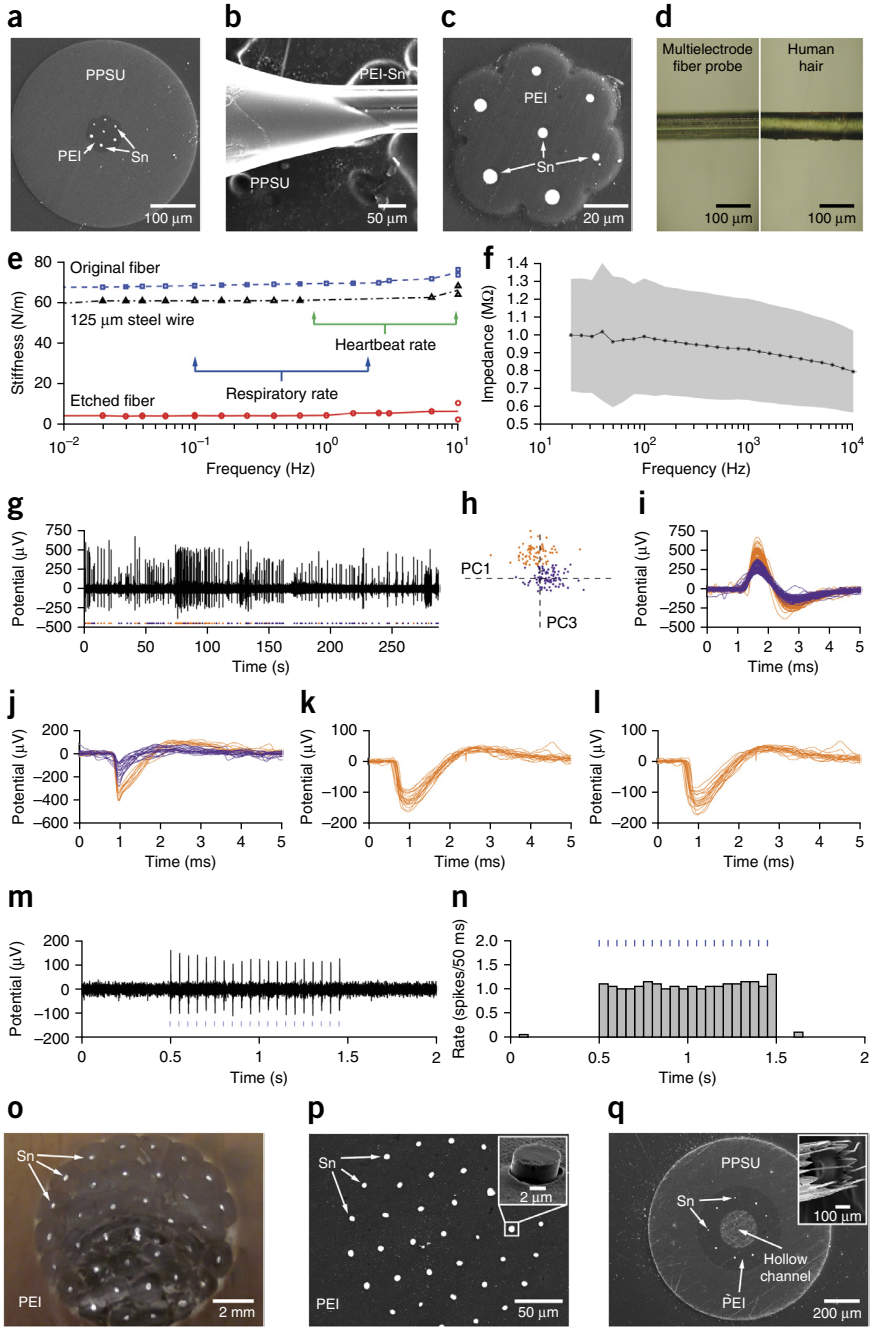

Figure 3 Multielectrode fiber probe fabrication and characterization. (**a**) Scanning electron microscopy (SEM) cross-sectional image of a multielectrode fiber with a diameter of 416 µm. (**b**–**d**) Selective etching of the sacrificial PPSU layer (**b**) exposes an array of tin electrodes within the PEI cladding and reduces the diameter to 85 µm (**c**), which is similar to that of a human hair (**d**). (**e**) Comparison of the bending stiffness of the multielectrode probes before (blue dashed line) and after (red solid line) selective etching of the cladding and the bending stiffness of a 125-µm steel microwire (black dashed-dotted line). (**f**) Impedance spectra for fiber electrodes ($n = 4$). (**g**) Spontaneous single-neuron activity recorded in the mPFC of an anesthetized WT mouse with a multielectrode probe. Orange and purple markers indicate time points of two different units. (**h**) PCA and *k*-means clustering performed on the trace in **g**. Two units are separable. (**i**) Extracted action-potential shapes of the two units in **g**. (**j**) Two units recorded on one of the electrodes of a chronically implanted multielectrode probe (as found by PCA and *k*-means clustering). (**k**,**l**) Units recorded by two other electrodes of the same probe. (**m**) Activity following optogenetic stimulation (5-ms pulse width, 20 Hz, 1 s) recorded in the mPFC of a *Thy1-ChR2-YFP* mouse with a multielectrode probe. Stimulation started at 0.5 s (dark blue lines indicate laser onsets). (**n**) PSTH analysis of 20 trials from **m** confirmed the reliability of the neuronal response. (**o**) Photograph of a multielectrode probe preform with 36 electrodes before the second drawing step. (**p**) SEM cross-sectional image of the probe produced from the preform in **o**. The inset shows an example electrode after etching of the cladding using O_2 plasma. (**q**) SEM image of a probe incorporating nine electrodes surrounding a hollow channel. The channel was filled with epoxy to facilitate cross-section polishing and SEM imaging. The inset shows exposed electrodes after O_2 plasma etching of the cladding. The channel was left open.

Using design I probes, we observed neural activity correlated with laser stimulation (jitter, 0.3 ms; peak latency, 5.9 ms) at a frequency of 10 Hz (λ = 473 nm, 5-ms pulse width, 3 mW/mm^2) (**Supplementary Fig. 6a**). We confirmed the stability of this finding by calculating peristimulus time histograms (PSTHs) (20 stimulation trials, 5-s intertrial interval) (**Supplementary Fig. 6b**). As a number of recording electrodes have been shown to exhibit optical artifacts[36], we confirmed that the evoked activity was of physiological origin by using high-frequency stimulation that yielded an uncorrelated response (**Supplementary Fig. 6c**,**d**).

Next we confirmed the long-term functionality of the fiber probes in freely moving adult *Thy1-ChR2-YFP* mice ($n = 4$) (**Fig. 2a**). Probes were implanted in the mPFC, and mice were subjected to neural recording and simultaneous optogenetic stimulation (as described above) 2 days, 1 week, 1 month and 2 months after implantation (**Fig. 2b**–**e**). Both recording and optical stimulation capabilities remained functional for 2 months. Furthermore, the polymer electrodes allowed for the recording of single-unit activity 1 month after implantation (**Fig. 2f**). Spike sorting revealed two neuronal units with good cluster-separation quality (L ratio < 10^{-5}, isolation distance = 422)[37] (**Fig. 2g**,**h**).

To demonstrate the drug-delivery capability of the implanted design I probes, we injected the AMPA receptor antagonist CNQX (0.1 mM, 33 nl/s, 2.5 µl)[38] into freely moving *Thy1-ChR2-YFP* mice (**Fig. 2i**–**k**). Prior to CNQX injection, we observed optically evoked activity (10 Hz, 5-ms pulse width, 3.9 mW/mm^2) (**Fig. 2i**), but CNQX injection diminished this activity (**Fig. 2j**). The response to optical stimulation recovered several minutes after the injection (**Fig. 2k**), and the post-injection activity waveform was indistinguishable from that observed before the injection (**Supplementary Fig. 7**). To demonstrate our ability to record neural activity during injection, we extracted the peak amplitude of each optically evoked response (R_{peak}) throughout the entire experiment (**Fig. 2l**,**m**). R_{peak} values 30 s after CNQX injection

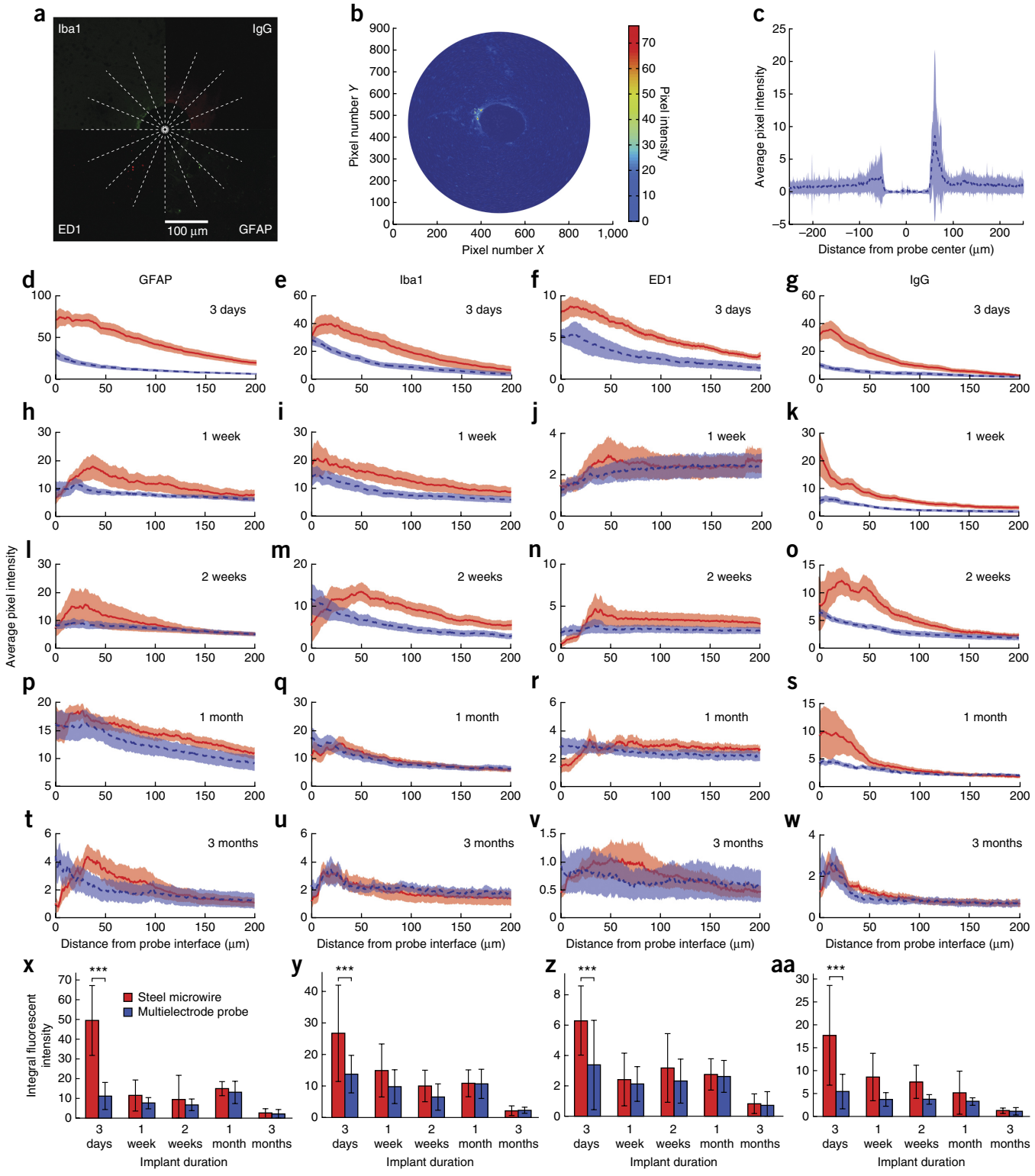

Figure 4 Tissue response to the multielectrode fiber probes. We quantified BBB breach (IgG) and the glial response (GFAP, Iba1, ED1) to chronically implanted multielectrode probes and microwires ($n = 6$ for each device and time point). (**a**) A combined panel of representative confocal images (20×) of the tissue surrounding a multielectrode probe 3 months after implantation. Such images were collected for each device, each time point and each marker (a total of 120 images were analyzed). (**b**) An example intensity plot corresponding to a marker IgG in **a** surrounding the entire implant interface (this procedure was performed for all 120 images). (**c**) An example of a marker IgG profile in **a** and **b** as averaged into a single trace (identical averaging performed on all 120 images). (**d**–**w**) For both multielectrode probes (blue line, average intensity; shaded area, s.e.m.) and microwires (red line, average intensity; shaded area, s.e.m.), the response is shown as a function of the distance from the device interface for each marker at each time point. (**d**,**h**,**l**,**p**,**t**) GFAP at 3 days (**d**), 1 week (**h**), 2 weeks (**l**), 1 month (**p**) and 3 months (**t**). (**e**,**i**,**m**,**q**,**u**) Iba1 at 3 days (**e**), 1 week (**i**), 2 weeks (**m**), 1 month (**q**) and 3 months (**u**). (**f**,**j**,**n**,**r**,**v**) ED1 at 3 days (**f**), 1 week (**j**), 2 weeks (**n**), 1 month (**r**) and 3 months (**v**). (**g**,**k**,**o**,**s**,**w**) IgG at 3 days (**g**), 1 week (**k**), 2 weeks (**o**), 1 month (**s**) and 3 months (**w**). (**x**–**aa**) The integral of fluorescent intensity 100 µm away from the implant interface (mean ± s.d.) for GFAP (**x**), Iba1 (**y**), ED1 (**z**) and IgG (**aa**) (***$P < 2 \times 10^{-6}$; one-way analysis of variance and Tukey's comparison test).

were significantly lower than those observed before infusion (67 ± 5 versus 126 ± 35, mean ± s.d., $P < 0.001$, $n = 3$) (**Fig. 2n**). We evaluated the microfluidic capabilities of design II probes similarly by injecting the $GABA_A$ receptor antagonist bicuculline methiodide through the hollow channel and assessing its effect on neural response to optical stimulation (**Supplementary Fig. 8**).

To our knowledge, our multimodality probes are the first example of an integrated all-polymer device suitable for combined long-term optogenetic and pharmacological interrogation and neural recording in freely moving mice.

Polymer-metal multielectrode fiber probes

In addition to flexibility, small device dimensions are correlated with improved performance and longevity of neural recordings[39]. Thus, we produced multielectrode array fibers with an individual electrode diameter of ~5 µm suitable for single-neuron recordings with high SNRs. To achieve this, we performed a two-step TDP[27] (**Supplementary Fig. 9**), which allowed for feature reduction by more than 40,000 times.

Using two macroscopic polymer (PEI and PPSU) cylinders and one tin rod, we produced >700 m of fiber incorporating seven tin electrodes (**Fig. 3a**) with uniform electrode diameters (5.1 ± 1.4 µm, mean ± s.d.) and spacing (23.3 ± 1.5 µm). The electrode spacing and dimensions were consistent with those defined during the initial preform fabrication. Selective etching of the PPSU cladding (**Fig. 3b**) resulted in substantial reduction of the probe diameter (from 416 to 85 µm; **Fig. 3c**) and allowed us to create probes with dimensions comparable to those of human hair (**Fig. 3d**) and a bending stiffness of 4–7 N/m, which is an order of magnitude less than that of the 125-µm steel microwires commonly used in electrophysiological recordings (**Fig. 3e**).

The impedance of the tin electrodes was within a useful range for extracellular recordings (892 ± 313 kΩ) (**Fig. 3f**)[40,41] and had spectra similar to those of commercial resistors (**Supplementary Fig. 10**). The latter suggests that impedance is dominated by resistance rather than capacitance for these electrodes.

In vivo electrophysiology with multielectrode fiber probes

To evaluate the general utility of the multielectrode probes for neural recordings, we used WT mice. *Thy1-ChR2-YFP* mice were used to test recording during optical stimulation.

In WT mice, analysis of the recorded traces revealed neural activity at the single-unit level, confirming the utility of the probes for neurophysiological recordings (**Fig. 3g–l**). Spike sorting (**Fig. 3g**) revealed two separable units with intermediate cluster separation quality (L ratio = 0.018, isolation distance = 20) (**Fig. 3h,i**). We also found that neural recordings could be performed simultaneously on multiple electrodes (**Fig. 3j–l**). Two separable units were recorded on one channel (L ratio = 2×10^{-4}, isolation distance = 38) (**Fig. 3j**) concomitantly with the recording of activity on two other channels (**Fig. 3k,l**).

After confirming the ability to record single action potentials with an SNR of 13 ± 6, we tested these devices in the presence of optical stimuli using a separate optical fiber. Evoked neural activity was correlated with light pulses at 20 Hz (jitter = 0.2 ms, peak latency = 4.1 ms, 1-s trial duration, 5-ms pulse width) (**Fig. 3m**). The reliability of this finding was assessed by PSTH analysis from 20 repetitions (5-s intertrial interval) (**Fig. 3n**). We confirmed the physiological nature of the response by increasing the stimulation frequency to 100 Hz (**Supplementary Fig. 11**), which led to a loss of synchrony akin to the result obtained with the multifunctional fibers.

Although tin is not commonly used in neural recording devices, our experiments demonstrate its utility for detecting single-unit activity. It is also possible to increase the number of electrodes in a device by changing the preform design (**Fig. 3o,p**). Furthermore, multielectrode polymer-metal fibers can be designed to incorporate additional modalities—for example, a probe with nine tin electrodes surrounding a microfluidic channel (**Fig. 3q**). The electrode-tissue interface can be improved if the device tip is subjected to to O_2 plasma etching, which allows further exposure of the electrodes from the PEI cladding (insets in **Fig. 3p,q**).

Foreign body response to fiber probes

To evaluate the biocompatibility of our multielectrode fiber probes, we compared the tissue response to our devices and to microwires using immunohistochemical analysis of brain slices 3 days to 3 months after implantation. The presence of immunoglobulin G (IgG) was used to assess the BBB breach, glial fibrillary acidic protein (GFAP) was used for astrocytic response, and ionized calcium-binding adaptor molecule 1 (Iba1) and cluster differentiation 68 (CD68/ED1/macrosialin) were markers for activated macrophages and microglia, respectively[19,42]. Tissue response was then quantified as a function of the distance from the electrode-tissue interface (**Fig. 4a–c**).

Multielectrode probes yielded significantly less foreign body response and BBB breaching (**Fig. 4d–g**) 3 days after implantation than did microwire electrodes ($P < 2 \times 10^{-6}$). This finding remained as a trend at longer implantation times for the astrocytic and microglial response and the amount of IgG in the surrounding tissue (**Fig. 4h–aa**). For both microwires and multielectrode probes, a significant ($P < 0.0001$) decrease in foreign body response was observed from 3 days to 3 months after implantation (**Fig. 4x–aa**), consistent with previous reports for microwires[19].

Similarly, multimodality fiber probes induced a negligible glial response but were associated with a greater amount of IgG, corresponding to a greater breach of the BBB consistent with their larger dimensions (**Supplementary Fig. 12**).

DISCUSSION

In this study we used the TDP to fabricate hundreds of meters of polymer-based neural probes with feature sizes as small as 5 µm and multimodal capabilities including simultaneous optogenetic stimulation, neural recording and drug delivery in freely moving mice. Our choice of polymers and a low-melting-temperature metal as fiber constituents allowed us to produce flexible devices that maintained functionality during bending, which may permit their future application in areas of the nervous system where significant deformations are caused by muscle movement.

The diameters of the probes fabricated in this study ranged from 70 to 700 µm; however, we have demonstrated that the overall dimensions of our devices can be further reduced by selective etching of sacrificial claddings (**Fig. 3a–d**, **Supplementary Fig. 13**). The electrode diameters in our multielectrode fibers were as small as 5 µm, but optimization of the process might allow further size reduction and an increase in the number of recording sites. Currently, the number and the dimensions of recording electrodes are limited primarily by the back-end connectorization procedures, rather than by the properties of the TDP.

Unlike lithographic fabrication approaches that require numerous steps, our process allows for the robust, inexpensive production of thousands of highly consistent multifunctional neural probes. However, in comparison to that of some commercially available probes, the recording capability of our devices is currently limited

to the tip because of the nature of the TDP. This challenge could potentially be overcome with additional post-processing, albeit with decreased fabrication throughput.

Although poorly understood, the foreign body response manifested in glial scarring and neuronal death is considered the key factor leading to the failure of chronically implanted neural probes[43–45]. Recently, limited reaction to metal microwires as compared to commonly used silicon-based probes was demonstrated, and the importance of chronic BBB breach to the tissue reaction has been suggested[19]. Compared to microwires, our multielectrode probes led to considerably less glial response and BBB breach 3 days after implantation and a reduced response for longer implantations (**Fig. 4**). Furthermore, the fiber probes did not cause any of the notable tissue accumulation or structural degradation commonly observed with microwires and silicon probes[18] (**Supplementary Figs. 14** and **15**). Future designs incorporating smaller features; softer, more biocompatible polymers; and potential surface modifications might further improve the long-term compatibility and functionality of fiber-based multimodal neural interfaces (**Supplementary Fig. 16**).

The TDP allowed for straightforward integration of low-loss optical waveguides (1.6–2.6 dB/cm) and neural recording electrodes within polymer-based fiber probes compatible with implantation and experiments in freely moving mice. Optical powers of <1 mW, easily accessible with diode-pumped solid-state laser modules, are sufficient to deliver at least 1 mW/mm^2, the power density threshold for ChR2-facilitated neural excitation[46], to the tip of a 5-cm-long fiber. Furthermore, the transmission spectra (**Fig. 1g**) indicate that our multimodality fiber probes can be used with other opsins such as inhibitory amber-light-sensitive halorhodopsin or green-light-sensitive archaerhodopsin variants (eNpHR3.0 (ref. 47) or eArch[48,49]).

In addition to optical interrogation, our fibers permit controlled fluid infusion through the integrated hollow channels, which allows for the delivery of drugs (as demonstrated in this study), viral vectors or cell-selective neurotoxins into neural tissues. Consequently, flexible polymer-based fiber probes could be used in biocompatible multifunctional tools for dynamic optogenetic mapping of neural circuits in freely behaving animals.

METHODS

Methods and any associated references are available in the online version of the paper.

Note: Any Supplementary Information and Source Data files are available in the online version of the paper.

ACKNOWLEDGMENTS

This work was supported in part by the National Science Foundation under a CAREER award to P.A. (CBET–1253890), the Center for Materials Science and Engineering (DMR-0819762), the Center for Sensorimotor Neural Engineering (EEC-1028725), the McGovern Institute for Brain Research, the US Army Research Laboratory and the US Army Research Office through the Institute for Soldier Nanotechnologies under contract number W911NF-13-D-0001, and a grant from the Simons Foundation to the Simons Center for the Social Brain at MIT. The authors are grateful to G. Feng for the generous donation of *Thy1-ChR2-YFP* mice, W. Jia and J. LaVine for initial help with microfluidic characterization and C. Moritz and L.H. Tsai for assistance with equipment.

AUTHOR CONTRIBUTIONS

P.A., Y.F. and U.P.F. designed the study. X.J. and A.C. drew multifunctional and multielectrode fibers, respectively. X.J. and J.S. connectorized multimodality probes. A.C. and C.M.T. connectorized and characterized multielectrode probes. C.L., L.W., X.J., C.H. and J.S. evaluated optical properties. A.C., C.M.T. and X.J. obtained electrode impedance spectra. A.C. conducted mechanical tests. X.J. and U.P.F. performed microfluidic characterization. U.P.F., A.C., X.J. and P.A. performed *in vivo* experiments. R.A.K., U.P.F., A.C., J.S. and C.M.T. investigated tissue response. U.P.F., A.C., R.A.K., X.J., Y.F. and P.A. analyzed the data and wrote the manuscript.

COMPETING FINANCIAL INTERESTS

The authors declare no competing financial interests.

1. Holtmaat, A. & Svoboda, K. Experience-dependent structural synaptic plasticity in the mammalian brain. *Nat. Rev. Neurosci.* **10**, 647–658 (2009).
2. Gradinaru, V., Mogri, M., Thompson, K.R., Henderson, J.M. & Deisseroth, K. Optical deconstruction of parkinsonian neural circuitry. *Science* **324**, 354–359 (2009).
3. Zhang, F., Aravanis, A.M., Adamantidis, A., de Lecea, L. & Deisseroth, K. Circuit-breakers: optical technologies for probing neural signals and systems. *Nat. Rev. Neurosci.* **8**, 577–581 (2007).
4. Ramirez, S. *et al.* Creating a false memory in the hippocampus. *Science* **341**, 387–391 (2013).
5. Znamenskiy, P. & Zador, A.M. Corticostriatal neurons in auditory cortex drive decisions during auditory discrimination. *Nature* **497**, 482–485 (2013).
6. Kravitz, A.V., Tye, L.D. & Kreitzer, A.C. Distinct roles for direct and indirect pathway striatal neurons in reinforcement. *Nat. Neurosci.* **15**, 816–818 (2012).
7. Anikeeva, P. *et al.* Optetrode: a multichannel readout for optogenetic control in freely moving mice. *Nat. Neurosci.* **15**, 163–170 (2012).
8. Rubehn, B., Wolff, S.B., Tovote, P., Luthi, A. & Stieglitz, T. A polymer-based neural microimplant for optogenetic applications: design and first *in vivo* study. *Lab Chip* **13**, 579–588 (2013).
9. Zhang, J. *et al.* Integrated device for optical stimulation and spatiotemporal electrical recording of neural activity in light-sensitized brain tissue. *J. Neural Eng.* **6**, 055007 (2009).
10. Campbell, P.K., Jones, K.E., Huber, R.J., Horch, K.W. & Normann, R.A. A silicon-based, three-dimensional neural interface: manufacturing processes for an intracortical electrode array. *IEEE Trans. Biomed. Eng.* **38**, 758–768 (1991).
11. Jog, M.S. *et al.* Tetrode technology: advances in implantable hardware, neuroimaging, and data analysis techniques. *J. Neurosci. Methods* **117**, 141–152 (2002).
12. Kennedy, P.R. The cone electrode: a long-term electrode that records from neurites grown onto its recording surface. *J. Neurosci. Methods* **29**, 181–193 (1989).
13. McNaughton, B.L., O'Keefe, J. & Barnes, C.A. The stereotrode: a new technique for simultaneous isolation of several single units in the central nervous system from multiple unit records. *J. Neurosci. Methods* **8**, 391–397 (1983).
14. Seymour, J.P., Langhals, N.B., Anderson, D.J. & Kipke, D.R. Novel multi-sided, microelectrode arrays for implantable neural applications. *Biomed. Microdevices* **13**, 441–451 (2011).
15. Borschel, G.H., Kia, K.F., Kuzon, W.M. & Dennis, R.G. Mechanical properties of acellular peripheral nerve. *J. Surg. Res.* **114**, 133–139 (2003).
16. Green, M.A., Bilston, L.E. & Sinkus, R. *In vivo* brain viscoelastic properties measured by magnetic resonance elastography. *NMR Biomed.* **21**, 755–764 (2008).
17. Ward, M.P., Rajdev, P., Ellison, C. & Irazoqui, P.P. Toward a comparison of microelectrodes for acute and chronic recordings. *Brain Res.* **1282**, 183–200 (2009).
18. Polikov, V.S., Tresco, P.A. & Reichert, W.M. Response of brain tissue to chronically implanted neural electrodes. *J. Neurosci. Methods* **148**, 1–18 (2005).
19. Saxena, T. *et al.* The impact of chronic blood–brain barrier breach on intracortical electrode function. *Biomaterials* **34**, 4703–4713 (2013).
20. Seymour, J.P. & Kipke, D.R. Neural probe design for reduced tissue encapsulation in CNS. *Biomaterials* **28**, 3594–3607 (2007).
21. Lee, H., Bellamkonda, R.V., Sun, W. & Levenston, M.E. Biomechanical analysis of silicon microelectrode-induced strain in the brain. *J. Neural Eng.* **2**, 81–89 (2005).
22. Kim, D.H. *et al.* Dissolvable films of silk fibroin for ultrathin conformal bio-integrated electronics. *Nat. Mater.* **9**, 511–517 (2010).
23. Kuo, J.T.W. *et al.* Novel flexible Parylene neural probe with 3D sheath structure for enhancing tissue integration. *Lab Chip* **13**, 554–561 (2013).
24. Minev, I.R., Moshayedi, P., Fawcett, J.W. & Lacour, S.P. Interaction of glia with a compliant, microstructured silicone surface. *Acta Biomater.* **9**, 6936–6942 (2013).
25. Takeuchi, S., Suzuki, T., Mabuchi, K. & Fujita, H. 3D flexible multichannel neural probe array. *J. Micromech. Microeng.* **14**, 104–107 (2004).
26. Goff, D.R. *Fiber Optic Reference Guide: a Practical Guide to Communications Technology* (Focal Press, 2002).
27. Yaman, M. *et al.* Arrays of indefinitely long uniform nanowires and nanotubes. *Nat. Mater.* **10**, 494–501 (2011).
28. LeChasseur, Y. *et al.* A microprobe for parallel optical and electrical recordings from single neurons *in vivo*. *Nat. Methods* **8**, 319–325 (2011).
29. Abouraddy, A.F. *et al.* Towards multimaterial multifunctional fibres that see, hear, sense and communicate. *Nat. Mater.* **6**, 336–347 (2007).
30. Merolli, A. *et al.* Response to polyetherimide based composite materials implanted in muscle and in bone. *J. Mater. Sci. Mater. Med.* **10**, 265–268 (1999).
31. Yalon, M., Goldberg, E.P., Osborn, D., Stacholy, J. & Sheets, J.W. Polycarbonate intraocular lenses. *J. Cataract Refract. Surg.* **14**, 393–395 (1988).
32. Khanarian, G. & Celanese, H. Optical properties of cyclic olefin copolymers. *Opt. Eng.* **40**, 1024–1029 (2001).

33. Aden, M., Roesner, A. & Olowinsky, A. Optical characterization of polycarbonate: influence of additives on optical properties. *J. Polym. Sci. B Polym. Phys.* **48**, 451–455 (2010).
34. Tye, K.M. & Deisseroth, K. Optogenetic investigation of neural circuits underlying brain disease in animal models. *Nat. Rev. Neurosci.* **13**, 251–266 (2012).
35. Arenkiel, B.R. *et al. In vivo* light-induced activation of neural circuitry in transgenic mice expressing channelrhodopsin-2. *Neuron* **54**, 205–218 (2007).
36. Cardin, J.A. *et al.* Targeted optogenetic stimulation and recording of neurons *in vivo* using cell-type-specific expression of channelrhodopsin-2. *Nat. Protoc.* **5**, 247–254 (2010).
37. Schmitzer-Torbert, N., Jackson, J., Henze, D., Harris, K. & Redish, A.D. Quantitative measures of cluster quality for use in extracellular recordings. *Neuroscience* **131**, 1–11 (2005).
38. Steenland, H.W., Liu, H. & Horner, R.L. Endogenous glutamatergic control of rhythmically active mammalian respiratory motoneurons *in vivo*. *J. Neurosci.* **28**, 6826–6835 (2008).
39. Kozai, T.D. *et al.* Ultrasmall implantable composite microelectrodes with bioactive surfaces for chronic neural interfaces. *Nat. Mater.* **11**, 1065–1073 (2012).
40. Ferguson, J.E., Boldt, C. & Redish, A.D. Creating low-impedance tetrodes by electroplating with additives. *Sens. Actuators A Phys.* **156**, 388–393 (2009).
41. Williams, J.C., Hippensteel, J.A., Dilgen, J., Shain, W. & Kipke, D.R. Complex impedance spectroscopy for monitoring tissue responses to inserted neural implants. *J. Neural Eng.* **4**, 410–423 (2007).
42. Lind, G., Linsmeier, C.E. & Schouenborg, J. The density difference between tissue and neural probes is a key factor for glial scarring. *Sci. Rep.* **3**, 2942 (2013).
43. Prasad, A. *et al.* Comprehensive characterization and failure modes of tungsten microwire arrays in chronic neural implants. *J. Neural Eng.* **9**, 056015 (2012).
44. Woolley, A.J., Desai, H.A. & Otto, K.J. Chronic intracortical microelectrode arrays induce non-uniform, depth-related tissue responses. *J. Neural Eng.* **10**, 026007 (2013).
45. Karumbaiah, L. *et al.* Relationship between intracortical electrode design and chronic recording function. *Biomaterials* **34**, 8061–8074 (2013).
46. Yizhar, O., Fenno, L.E., Davidson, T.J., Mogri, M. & Deisseroth, K. Optogenetics in neural systems. *Neuron* **71**, 9–34 (2011).
47. Gradinaru, V. *et al.* Molecular and cellular approaches for diversifying and extending optogenetics. *Cell* **141**, 154–165 (2010).
48. Chow, B.Y. *et al.* High-performance genetically targetable optical neural silencing by light-driven proton pumps. *Nature* **463**, 98–102 (2010).
49. Mattis, J. *et al.* Principles for applying optogenetic tools derived from direct comparative analysis of microbial opsins. *Nat. Methods* **9**, 159–172 (2012).

ONLINE METHODS

Multimodality fiber probe fabrication. To fabricate design I multimodality probes, we rolled several cyclic olefin copolymer (COC; TOPAS) sheets and polycarbonate (PC; Ajedium Films) sheets around a 16-mm-thick PC rod and annealed, forming a single, solid preform. Four rectangular grooves were machined into the resulting cylinder, two of which were filled with conductive polyethylene (CPE; Hillas Packaging), after which we rolled PC, COC, and additional PC sheets, in that order. In contrast, design II was fabricated by rolling COC and PC sheets around a ceramic mandrel instead of a PC rod, and all four machined grooves were filled with CPE. The preforms were annealed at 190 °C to form a solid cylinder and then subjected to the TDP at 240 °C.

The electrodes were connected to external wires with conductive silver paint (SPI Supplies) after the outer cladding had been removed to expose the conductive polymer. The wires were then soldered to a custom-printed circuit board with a connector compatible with a zero insertion force clip. Similarly, we connected the fluidic channels by exposing a channel and then inserting the device perpendicularly through a section of ethylene-vinyl acetate tubing (0.5 mm inner diameter, McMaster-Carr) and gluing it in place. We connected the waveguide in the probes by inserting the tip of the probe into a 2.5 mm stainless steel ferrule (Thorlabs), gluing it in place and then polishing the surface (**Supplementary Fig. 16**).

Multielectrode probe fabrication. To fabricate multielectrode probes, we chose poly(etherimide) (PEI) and poly(phenylsulfone) (PPSU) rods (1.25 inch or 1.5 inch diameter; McMaster-Carr) as cladding and tin (Sn; Puratronic tin rods, 6 mm diameter, Alfa Aesar) as the electrode material. The polymer rods were cut into 8-inch-long sections and annealed in a vacuum oven (150 °C). We then machined a 0.25-inch hole in a PEI cylinder (1.25 to 1.5 inches in diameter) and filled it with a tin rod. The resulting first preform was then thermally drawn at 300–325 °C.

We prepared the second preform by filling a machined hole in a similar PPSU cylinder with a bundle of 6-inch-long fiber sections cut from the fiber obtained from the first drawing step. To eliminate air pockets between individual fiber strands, we annealed this second preform (250 °C in vacuum) before the second drawing step. We removed the outer PPSU layer afterward by dipping the fiber in tetrahydrofuran for 25 min. We established the connection to the tin electrodes in the multielectrode probe by first removing the polymer cladding from a section of the fiber using O_2 plasma and then individually connecting the exposed electrodes to a custom-printed circuit board with conductive silver paint.

Cross-section imaging. To image multimodality probes, we prepared the samples with a cross-section polisher (SM-Z04004T, JEOL, Peabody, MA) before imaging (Axioskop 2 in transmission mode, Carl Zeiss MicroImaging, Inc.). To image multielectrode probes, we fixed the samples in an epoxy matrix and polished the epoxy with a series of sandpapers with decreasing grain sizes, finishing with a 0.3 µm alumina particle solution. The samples were then sputter coated (Polaron Range) with a gold film (~5 nm) before imaging (scanning electron microscopy, 6010LA, JEOL).

Impedance spectroscopy. We measured the electrode impedance with a precision LCR meter (HP4284A, Agilent Technologies) with a sinusoidal input (10 mV, 20 Hz–10 kHz).

Mechanical properties. We characterized the bending stiffness with a dynamic mechanical analyzer (Q800, TA Instruments). Samples 1.2 cm in length were mounted with a single cantilever clamp. The samples were then tested with a frequency sweep (0.01–10 Hz) under controlled displacement (50 µm) at 37 °C.

Optical properties. To determine the optical transmission loss, we coupled a laser beam to the optical waveguide. The light output for different fiber lengths was measured with a photodetector (S121C, 400–1100 nm, 500 mW, Thorlabs) attached to a power meter (PM100D, Thorlabs). To test the performance of the waveguide while bent, we fixed one end of a fiber section and attached the other end to a moving stage (PT3, Thorlabs), and then we varied the distance between the two ends (**Supplementary Fig. 5**).

Microfluidic channels. To confirm the reliability of the fluidic channels of the multimodality probes, we connected the probes to a syringe controlled by an injection system (NanoFil syringe, UMP-3, Word Precision Instruments) through ethylene-vinyl acetate tubing (0.5 mm inner diameter, McMaster-Carr). We injected water (9 µl; target injection rates (nl/s): 1, 10, 20, 50, 80, and 100) and measured the injection output by weight. We calculated the injection rate by dividing the calculated injected volume by the time required to inject it.

***In vivo* electrophysiology.** All procedures involving animals were approved by the MIT Committee on Animal Care.

Multimodality and multielectrode fiber probes were tested in male WT mice (C57Bl/6, 8 weeks old, The Jackson Laboratories) or 9- to 10-week-old *Thy1-ChR2-YFP* mice (generously donated by G. Feng) housed at the MIT central animal facilities (12 h light/dark cycle, 22 °C, food and water *ad libitum*). No animals were excluded from the analysis. Because of the technical nature of the study, no blinding was done.

We performed surgeries on deeply anesthetized mice (in mg/kg bodyweight: ketamine, 100; xylazine, 10; in saline) positioned in a stereotactic frame (David Kopf Instruments).

To facilitate insertion of the probes into the brain, we cut the tips of the multimodality probes at an angle of ~60°. Connection to an RZ5D (Tucker Davis Technologies) recording system was established through a PZ2-32 headstage with a 16-channel zero insertion force–clip headstage (Tucker Davis Technologies), and probes were positioned within the medial prefrontal cortex (mPFC; coordinates from bregma (in millimeters): rostrocaudal (RC), 1.8; mediolateral (ML), −0.4; dorsoventral (DV), −1.7).

For optogenetic stimulation in *Thy1-ChR2-YFP* mice, we used a 50 mW 473 nm diode-pumped solid-state laser (OEM Laser Systems) coupled to the internal fiber waveguide (if applicable) or a silica fiber (300 µm core, Thorlabs) for separate stimulation. Stimulation frequencies were controlled using the RZ5D system (10, 20, 100 Hz; 5 ms pulse width, 1 s trial duration, 5 s intertrial interval).

Recordings under acute conditions were performed with a wire in the neck used as a ground and were referenced to a channel without apparent electrophysiological signals. If mice were implanted for chronic recordings, a stainless steel screw was inserted into the skull above the cerebellum as a ground and reference, and then the implant and skull coverage were fixed with dental acrylic (Metabond, Parkell; Jet-Set 4, Lang Dental) and mice were returned to their home cages for recovery.

Signals were filtered (0.3–5 kHz) and digitized (~50 kHz sampling frequency). Data analysis was performed with Matlab (The Mathworks). We performed spike sorting by detecting spikes with an amplitude threshold and a deadtime of 1 ms to exclude double detections. The detected spikes were visually confirmed and then subjected to a principal component analysis followed by *k*-means clustering[50]. We assessed the quality of the clustered data by calculating the *L* ratio and the isolation distance of detected clusters[37]. The signal-to-noise ratio was calculated by dividing the mean of the R_{peak} of the detected spikes by three times the standard deviation of the noise[19].

To confirm the ability to deliver drugs into the brain, we injected the α-amino-3-hydroxy-5-methyl-4-isoxazole propionic acid (AMPA) receptor antagonist 6-cyano-7-nitroquinoxaline-2,3-dione (CNQX) (0.1 mM, 33 nl/s, 2.5 µl) through one of the channels of the design I multimodality probes up to 1 week after implantation. We analyzed data by extracting the R_{peak} of the detected spikes, which revealed three distinct response phases. Average R_{peak} values of these 30 s phases (before, 30 s before the start of an injection; after, 20 s after the termination of an injection; recovery, 1,600 s after the end of an injection) were compared across different recordings ($n = 3$). The significance of the findings was assessed by Student's *t*-test as implemented in Matlab.

Long-term tissue response assessment. To compare long-term tissue responses, we implanted WT mice ($n = 10$ mice; 2 mice per time point) with three ipsilateral multielectrode probes and three contralateral microwires. (Coordinates from bregma (in millimeters), probe/microwire 1: RC, 1.8; ML, ±0.4; DV, −5. Probe/microwire 2: RC, 0.4; ML, ±2.5; DV, −5. Probe/microwire 3: RC, −2.1; ML, ±1; DV, −5.) To this end, we stiffened multielectrode probes for insertion by coating them with melted poly(ethylene glycol) (PEG; 3000 MW, Fluka). Implantation

and recovery procedures were analogous to the implantation of multimodality probes. Implanted animals were anesthetized and transcardially perfused with saline followed by 4% paraformaldehyde in PBS (3 days, 1 week, 2 weeks, 1 month, and 3 months after implantation). The devices were carefully explanted before the brains were removed and fixed in 4% paraformaldehyde in PBS overnight at 4 °C. Explants were imaged (multimodality probes, Nikon eclipse e600 POL microscope, **Supplementary Fig. 14**; multielectrode probes, 6010LA scanning electron microscope, **Supplementary Fig. 15**). Brains were sectioned in the horizontal plane at 50 µm on a vibrating blade microtome (Leica VT1000S). Free-floating sections were washed in PBS and incubated in a blocking solution consisting of 0.3% Triton X-100 (vol/vol) and 1.5% goat serum (vol/vol; Sigma) in PBS. Slices were then incubated for 2 days at 4 °C with primary antibodies in blocking solution (goat anti-GFAP, 1:1,000, Abcam; goat anti-Iba1, 1:500, Abcam; rabbit anti-CD68, 1:250, Abcam). Sections were washed three times with PBS for 30 min and then stained for 2 h at 20 °C with corresponding secondary antibodies (donkey anti-goat, goat anti-rabbit, or goat anti-mouse IgG was conjugated to either Alexa Fluor 488 or Alexa Fluor 633 (Life Technologies), all at 1:1,000). Slices were washed three times with PBS and incubated with DAPI (4′6-diamidino-2-phenylindole) (1:50,000) for 30 min. Sections were washed a final time and mounted on Superfrost microscope slides (VWR) with PVA-Dabco (Sigma). All fluorescent images were acquired at the same exposure settings with a laser scanning confocal microscope (Olympus FV1000) with an oil immersion 20× objective with a numerical aperture NA = 1.25 unless otherwise noted. Tissue response to design I multimodality probes was imaged with a 10× air objective (**Supplementary Fig. 12**).

Two sections per mouse were acquired between 3.5 and 5 mm DV for each microwire/probe. Fluorescent intensity as a function of distance from the electrode-tissue interface for IgG, GFAP, Iba1, and ED1 was calculated with Matlab and the Image Processing Toolbox (**Fig. 4a**), similar to previously described methods[19,42]. Fluorescence intensity values were found from 180 equidistant, radial lines centered at the middle of the implant void (**Fig. 4b**) and averaged for each image (**Fig. 4c**). Averaged traces were compiled for both microwire and multielectrode fibers for each time point (**Fig. 4d–w**). Statistical significance was assessed in Matlab, first by confirming a normal distribution (Lilliefors test) and then by one-way analysis of variance and Tukey's honestly significant difference (HSD) criterion.

50. Quian Quiroga, R., Nadasdy, Z. & Ben-Shaul, Y. Unsupervised spike detection and sorting with wavelets and superparamagnetic clustering. *Neural Comput.* **16**, 1661–1687 (2004).

doi:10.1038/nbt.3093